Journal of Alloys and Compounds 695 (2017) 1976–1983

Contents lists available at ScienceDirect

Journal of Alloys and Compounds

journal homepage: http://www.elsevier.com/locate/jalcom

Fabrication, microstructure and mechanical properties of W–NiTi composites

Yang Shao [a, **], Fangmin Guo [a], Yong Huan [b], Daqiang Jiang [a], Junsong Zhang [a], Yang Ren [c], Lishan Cui [a, *]

[a] State Key Laboratory of Heavy Oil Processing and Department of Materials Science and Engineering, China University of Petroleum, Beijing 102249, China
[b] State Key Laboratory of Nonlinear Mechanics (LNM), Institute of Mechanics, Chinese Academy of Sciences, Beijing 100190, China
[c] X-ray Science Division, Argonne National Laboratory, Argonne, IL 60439, USA

ARTICLE INFO

Article history:
Received 25 April 2016
Received in revised form
23 October 2016
Accepted 2 November 2016
Available online 4 November 2016

Keywords:
Martensite variant detwinning
Tungsten
Infiltration
Near equiatomic NiTi

ABSTRACT

New two-phase tungsten-based composites containing 88 wt% tungsten powders and 12 wt% nearly equiatomic NiTi alloy deforming by martensite variant detwinning were fabricated by infiltration and hot pressing in this study. The change of Ti/Ni ratio in NiTi mater alloy and the effect of addition of Nb element on the microstructure, martensitic transformation and mechanical properties of W–NiTi composites were investigated by comparison of W–$Ni_{50}Ti_{50}$, W–$Ni_{44}Ti_{56}$, W–$Ni_{42}Ti_{58}$ and W–$Ni_{42}Ti_{53}Nb_5$ composites. The results showed that brittle Ni_3Ti formed in the W–$Ni_{50}Ti_{50}$ and W–$Ni_{44}Ti_{56}$ composites and brittle Ti_2Ni formed in the W–$Ni_{42}Ti_{58}$ composites while no brittle intermetallics formed in the W–$Ni_{42}Ti_{53}Nb_5$ composite. The W–$Ni_{42}Ti_{53}Nb_5$ composite exhibited the sharpest martensitic transformation with the largest transformation enthalpy among the four different composites. The W–$Ni_{42}Ti_{53}Nb_5$ composite exhibited a double-yielding phenomenon under compression with an ultimate compressive strength of 3820 MPa and a deformation of 50.4%. *In-situ* synchrotron high-energy X-ray diffraction measurements revealed the first yielding was caused by the martensite reorientation of the NiTi matrix and the second was due to the commencement of massive plastic deformation of the reoriented martensite and is also attributed to the microscopic internal fracturing of the W particles.

1. Introduction

Tungsten (W) is widely used in military and industry applications due to its attractive physical properties: high melting point (3420 °C), high mass density, good thermal conductivity and comparatively low activation under neutron irradiation [1]. However, the major disadvantage of tungsten is its ceramic-like brittle behavior and poor workability at room temperature, which restrict its structural applications [2]. To answer this challenge, the concept of developing composite microstructures by combining tungsten with ductile phases has been developed, through which an improvement in ductility at room temperature has been obtained in several kinds of tungsten based composites [3–5], especially for the well-known two-phase tungsten heavy alloys [6–9]. It is generally accepted that the ductile phases in these composites can effectively reduce the stress concentration ahead of the crack tip and slow down the propagation of cracks by plastic deformation [10–15]. Previous reports have shown that ductile alloys deforming by martensite variant detwinning also have the ability to reduce the stress concentration and prohibit crack propagation in composites [16]. Several kinds of composites containing brittle intermetallics or metallic glasses and ductile phases deforming by martensite variant detwinning with enhanced performance have been developed [16–20]. In this study, hence we report a new two-phase tungsten-based composite composed of brittle W particles embedded in a martensite matrix, where the ductile component deforms by martensite variant detwinning.

It is noted that nearly equiatomic NiTi alloy has excellent mechanical properties due to martensitic transformation or stress induced martensitic detwinning under loading, which is an excellent candidate as a component in composites [21,22]. While W, due to its high strength and no other intermetallics forming between W and NiTi phases [23,24], is always used as a reinforcement phase to improve the strength of NiTi alloy [25,26]. Naturally, it is reasonable

* Corresponding author.
** Corresponding author.
E-mail addresses: shaoyangok@163.com (Y. Shao), lscui@cup.edu.cn (L. Cui).

http://dx.doi.org/10.1016/j.jallcom.2016.11.032
0925-8388/

to expect that a W–NiTi composite composed of ductile NiTi and W particles with high strength and ductility overcomes the brittleness at room temperature.

As tungsten is refractory material, melting of tungsten is extremely difficult. Tungsten-based composites are always processed through powder metallurgy using element powders [6]. However, this may be not a feasible method to fabricate W–NiTi composites because of the composition sensitivity of martensitic transformation of NiTi alloys. As we all known, only nearly equiatomic NiTi alloy could undergo martensitic transformation or stress induced martensitic detwinning under loading [21] and the phase transformation characteristics of NiTi alloy are extremely sensitive to the composition of alloy [27]. A little variation in the ratio of the two elements might result in a large difference in the transformation temperatures and can lead to the formation of brittle intermetallics [28–31]. For Ti-rich alloys (around 50 at% Ni), stable Ti_2Ni appears in NiTi alloy due to little solubility for Ti in excess of 50 at.% [28]. While for Ni-rich alloys, precipitation proceeds through a series of phases: $Ti_3Ni_4 \rightarrow Ti_2Ni_3$ until finally the stable Ni_3Ti phase is reached [28,29]. However, the change in the Ti/Ni ratio is inevitable because of mutual diffusion between NiTi and W [32]. In order to reduce the composition sensitivity of martensitic transformation of nearly equiatomic NiTi alloy, a small amount of Nb could be added to the NiTi matrix [33]. Previous reports have revealed that the Nb element is dissolved more in Ti site than in Ni site in Ni-rich (around 50 at% Ni) NiTi alloys [33,34]. The maximum content of Nb dissolved in Ni-rich NiTi can even reach 6 at.% in previous report [35]. For Ti-rich (around 50 at.% Ti) NiTi alloys, the addition of Nb could result in precipitation of Nb-rich phase in NiTi matrix [36]. Since Ti and Nb have complete solubility in the Ti–Nb binary system [37], the rest Ti element in Ti-rich alloys forms solid solution with Nb and the maximum content of Ti dissolved in Nb-rich phase is even more than 12 at.% [37,38]. Hence, the addition of Nb could greatly increase the Ti/Ni ratio change in NiTi alloy, avoiding the presence of brittle phases in binary NiTi alloys caused by the change of Ti/Ni ratio.

In this study, new tungsten based composites, W–NiTi systems, were prepared by infiltration and hot pressing process. The effect of NiTi composition and the addition of Nb element on the microstructure, martensitic transformation behavior of W–NiTi composites were investigated in order to obtain ductile NiTi matrix in the composite. The microscopic deformation mechanism was studied by using *in situ* synchrotron-based high-energy X-ray diffraction (HEXRD) under quasi-static compression.

2. Experiments

Four master alloys with different nominal compositions of $Ni_{50}Ti_{50}$, $Ni_{44}Ti_{56}$, $Ni_{42}Ti_{58}$ and $Ni_{42}Ti_{53}Nb_5$ were prepared from high-purity components (purity 99.8 wt %) by arc melting under a Ti-gettered argon atmosphere. Highly pure W powders with particle size in the range of 2–6 μm were purchased from Zhuzhou Kete Industries Co., Ltd. The desired composition of the W–NiTi composites contains 88% W in mass fraction, which was in the range of the conventional two-phase tungsten-based composites (containing 80 to 98 wt% tungsten) [39]. The W–NiTi composites were synthesized by two steps in a vacuum hot-pressing furnace. Firstly, W powders, NiTi (Nb) alloy and a graphite punch were successively placed into a graphite die of 20 mm internal diameter. Then the graphite die was heated to 1350 °C at a rate of 10 °C/min in the vacuum hot-pressing furnace. The infiltration process was carried out at 1350 °C, which was higher than the melting of NiTi [21], for 30 min in argon atmosphere and then the samples were cooled in the furnace down to 1200 °C at a rate of 10 °C/min. After holding for 5 min at this temperature, a pressure of 30 MPa was applied on the samples and kept for 5 min. Then the heating source was switched off and the sample was cooled down to room temperature in the furnace. Fig. 1 (a) and (b) shows the schematic illustration of the preparation procedure and the typical sintering and hot pressing cycle for W–NiTi composites, respectively.

The specimens were grounded and polished to remove surface contamination from graphite and all the samples were cut near the center part of the as-fabricated composites. Densities of the composites were measured by Archimedes water immersion technique. The microstructure of the as-fabricated composites was characterized by transmission electron microscopy (TEM, FEI F20) and scanning electron microscopy (SEM, FEI Quanta 200F) equipped with an energy dispersive X-ray analyzer (EDX). The phase component was characterized by means of X-ray diffraction (XRD, Bruker AXS D8) using Cu K_α radiation. The transformation behavior was measured by differential scanning calorimetry (DSC, TA Q20) under nitrogen gas flow at heating and cooling rates of 10 °C/min. The compression tests were performed using cylindrical specimens with dimensions of φ4 mm × 8 mm height using a servo-hydraulic materials testing system (MTS 810) with an extensometer at a strain rate of 5×10^{-4} s^{-1} at room temperature. In situ synchrotron high-energy X-ray diffraction (HEXRD) measurements during compression were performed using cylindrical specimens with dimensions of φ1.2 mm × 1.8 mm height at room temperature using a self-designed device at the 11-ID-C beam line of the Advanced Photon Source at Argonne National Laboratory in USA. High-energy X-rays with a beam size of 0.8 mm × 0.8 mm and wavelength of 0.11165 Å were used to obtain two-dimensional (2D) diffraction patterns in transmission geometry. One-dimensional (1-D) HEXRD diffraction patterns under various applied stresses were obtained by integrating along the specified azimuthal angle over a range of ±10° in the 2-D diffraction patterns using the FIT2D software package [40].

3. Results and discussion

As-fabricated W–NiTi composites with different master alloys

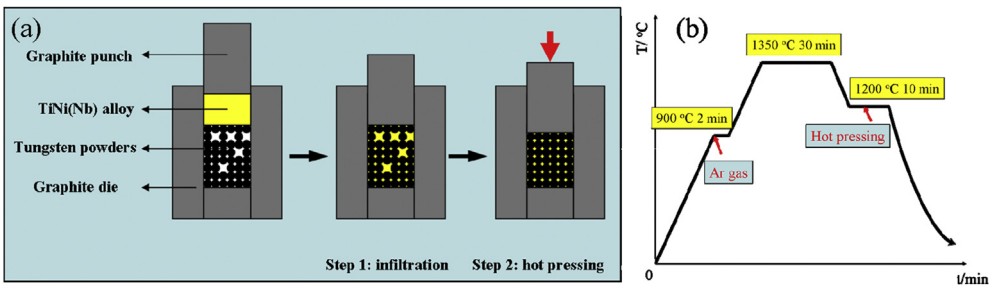

Fig. 1. (a) Schematic illustration of preparation procedure. (b) Typical sintering and hot pressing cycle for W–NiTi composites.

were first examined by XRD to determine the exact phase constituents in the composites. The diffraction patterns of samples are shown in Fig. 2. The strongest diffraction peaks in all of samples were that for W phase, which was related to the high W proportion in the composites (88% in mass fraction). The W–$Ni_{50}Ti_{50}$ sample contained not only B19'–NiTi phases but also brittle Ni_3Ti phase. The diffraction peaks of B19'–NiTi phases were much weaker than those of Ni_3Ti phase, which suggested that a large mount of Ni_3Ti phase formed. The formation of Ni_3Ti intermetallic compound may be related to the mutual diffusion between NiTi and W particles and

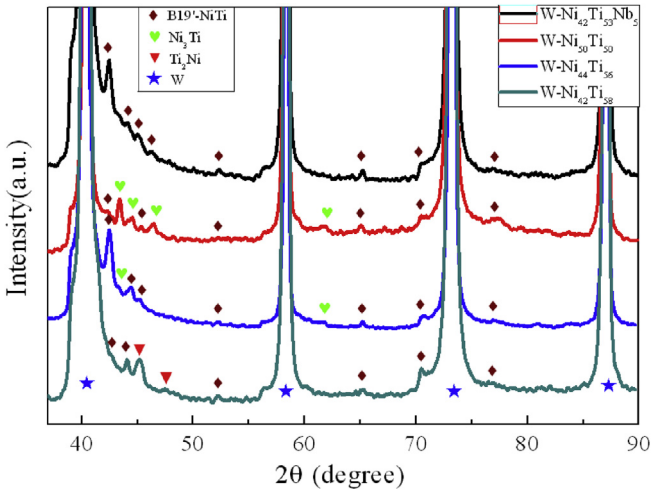

Fig. 2. XRD patterns of the as-fabricated W–NiTi composites with different master alloys.

the content of Ti dissolved in W particles was more that of Ni [32]. When the Ti/Ni ratio increased to 56: 44, the diffraction peaks of Ni_3Ti becoming weaker, suggesting the mount of brittle Ni_3Ti becoming smaller than that of the W–$Ni_{50}Ti_{50}$. With further increase of the Ti/Ni ratio to 58: 42, the diffraction peaks of Ni_3Ti disappeared and new peaks appeared at $2\theta = 41.59^\circ$ and 45.32° for W–$Ni_{42}Ti_{58}$ composite compared with that of the W–$Ni_{44}Ti_{56}$ composite, which matched with the peaks of Ti_2Ni phase [41]. This may be caused by the limit of solubility of Ti element in W phase. While for W–$Ni_{42}Ti_{53}Nb_5$ composite, only B19'–NiTi phases except for W were detected. No diffraction peaks of brittle Ti_2Ni and Ni_3Ti phases were found.

The microstructure of the samples sintered with different master alloys was analyzed by SEM. The results are presented in Fig. 3. It can be seen that for the W–$Ni_{50}Ti_{50}$ composite, the composite consists of gray area, dark area and white area. They were confirmed to be nearly equiatomic NiTi phase (dark area), Ni_3Ti phase (gray area) and W phase (white particles) respectively by the EDX analysis. A mass of Ni_3Ti formed in the as-fabricated W–$Ni_{50}Ti_{50}$ composite. While for samples of W–$Ni_{42}Ti_{53}Nb_5$ and W–$Ni_{44}Ti_{56}$ composites, they were composed of only nearly equiatomic NiTi matrix and W particles. When the Ti: Ni ratio raised to 58: 42, small amount of Ti_2Ni remained in NiTi matrix, as seen from Fig. 3(d). Meanwhile the density of the as-fabricated W–$Ni_{42}Ti_{53}Nb_5$ composite was 15.27 g/cm^3 (98.6% of theoretical density) measured by the Archimedes water immersion method.

The compositions of the NiTi matrix (point A) and the tungsten particles (point B and point C) in the as-fabricated W–$Ni_{42}Ti_{53}Nb_5$ composite analyzed by EDX were given in Table 1. Thus, the analysis shows that the matrix consisted of nearly equiatomic NiTi in the as-fabricated W–NiTi composite and NiTi and W phase were miscible. The Ti concentration in the tungsten particles was larger than that

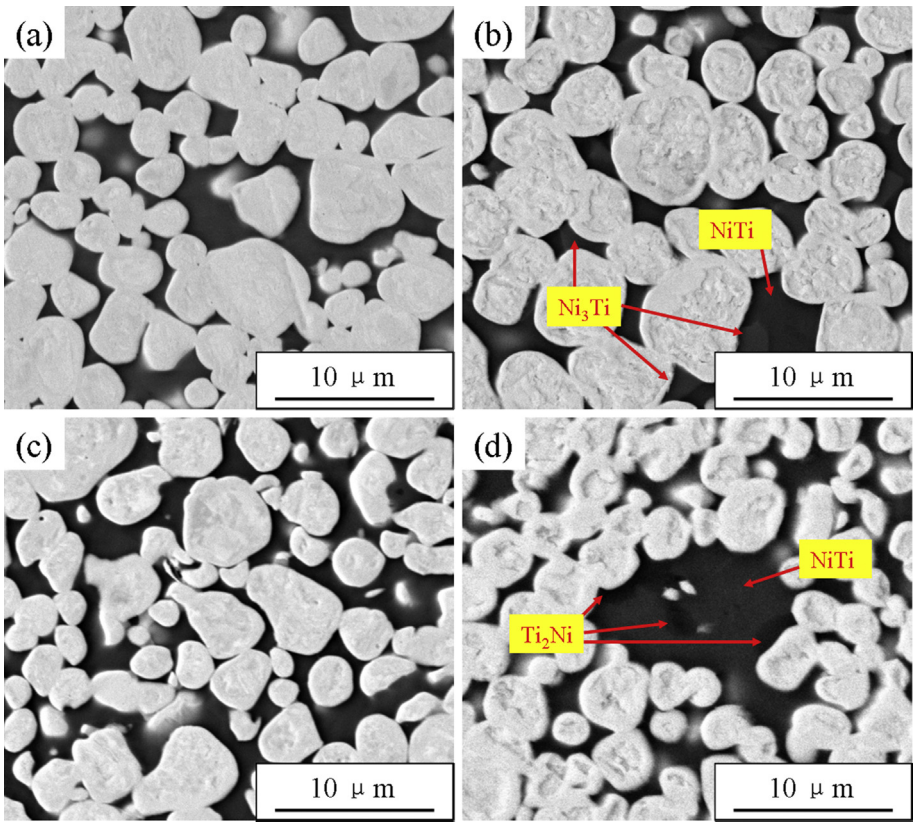

Fig. 3. Back scattering SEM micrographs of the W–NiTi composites with different master alloys (a) W–$Ni_{42}Ti_{53}Nb_5$, (b) W–$Ni_{50}Ti_{50}$, (c) W–$Ni_{44}Ti_{56}$ and (d) W–$Ni_{42}Ti_{58}$.

Table 1
Concentration of elements at different positions in the as-fabricated W–$Ni_{42}Ti_{53}Nb_5$ composite.

Positions	Concentration of elements (at.%)			
	W	Ni	Ti	Nb
Point A (NiTi matrix)	0.83	49.28	49.04	0.85
Point B (center of W particle)	97.50	0.00	2.50	0.00
Point C (edge of W particle)	80.59	4.47	10.97	3.97

of Ni, which was consistent with previous report [32]. This is further confirmed by the elemental mapping carried out by EDX analysis (Fig. 4(b)-(e)). Since this diffusion process consumed more Ti than Ni, it shifted the composition of equiatomic NiTi master alloy to higher Ni values and resulted into brittle Ni_3Ti phase in the W–$Ni_{50}Ti_{50}$ composite.

It is also noted that the results suggested that NiTi and W phase can dissolve each other, but the solubility of W in NiTi phase is limited to <2 at. % [42]. The dissolved W in NiTi phase has only small influences on the transformation temperatures and transformation hysteresis of NiTi alloy [26,43]. The NiTi matrix with W dissolved can undergo reversible martensitic transformation under thermal or mechanical loading cycles, which could be further confirmed by the DSC results shown in Fig. 5.

Fig. 5 shows the DSC curves of the sample sintered with different master alloys. As seen in Fig. 5, all the as-fabricated composites showed reversible martensitic transformations. The temperature regions of the reverse martensitic transformations of the W–$Ni_{50}Ti_{50}$ and W–$Ni_{44}Ti_{56}$ composites were much wider than that of the W–$Ni_{42}Ti_{53}Nb_5$ composite. It could be caused by the gradient change of Ti/Ni ratio resulting from the mutual dissolution between NiTi and W particles and the composition sensitivity of martensitic transformation of NiTi alloy. It also suggested that the addition of Nb element could decrease the composition sensitivity of martensitic transformation of NiTi alloy and effectively narrows the transformation temperature range. The DSC peaks that correspond to the martensitic phase transformations in the W–$Ni_{50}Ti_{50}$, W–$Ni_{44}Ti_{56}$ and W–$Ni_{42}Ti_{58}$ composites were smaller than those in the W–$Ni_{42}Ti_{53}Nb_5$ composite. The reason is that the presence of brittle intermetallics in the W–$Ni_{50}Ti_{50}$, W–$Ni_{44}Ti_{56}$ and W–$Ni_{42}Ti_{58}$ composites reduced the volume fraction of ductile NiTi that could undergo martensitic transformation during thermal cycles. The martensite transformation enthalpies (Δ H) of the four different W–NiTi composites were listed in Table 2. The W–$Ni_{42}Ti_{53}Nb_5$ composite exhibited the largest transformation enthalpy (i.e., 2.21 J/g). It has been known that the value of ΔH of as-cast NiTi

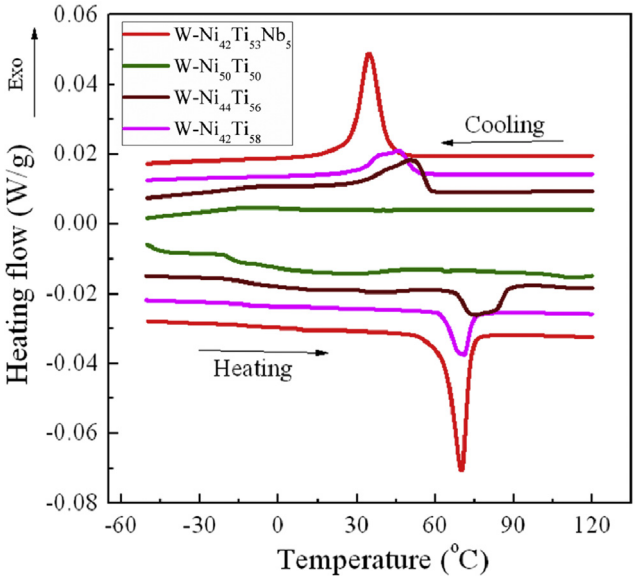

Fig. 5. Transformation behaviors of W–NiTi composites sintered with different master alloys.

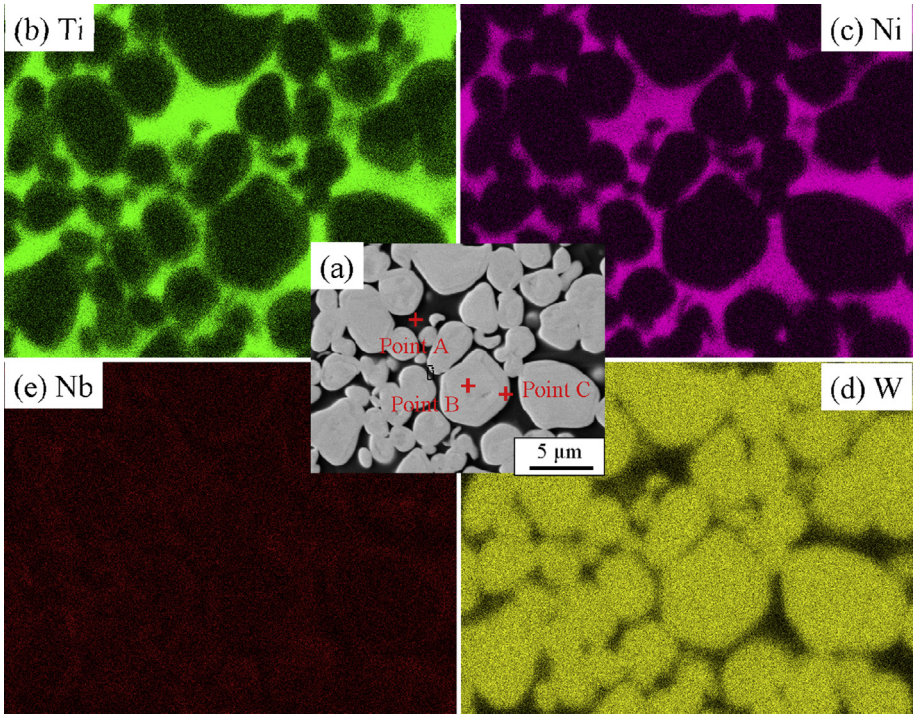

Fig. 4. Elemental mapping of the W–$Ni_{42}Ti_{53}Nb_5$ composites: (a) Back scattering SEM micrograph, (b) Ti, (c) Ni, (d) Nb and (e) W.

Table 2
Phase components and transformation measurements for W–NiTi composites.

W–NiTi composites	Phase components	Transformation EnthalpyΔH (J/g)	Calculated NiTi content (wt.%)
W–$Ni_{50}Ti_{50}$	W + B19'–NiTi + mass Ni_3Ti	1.482	6.74%
W–$Ni_{44}Ti_{56}$	W + B19'–NiTi + minor Ni_3Ti	1.746	7.94%
W–$Ni_{42}Ti_{58}$	W + B19'–NiTi + Ti_2Ni	1.446	6.57%
W–$Ni_{42}Ti_{53}Nb_5$	W + B19'–NiTi	2.21	10.05%

alloy was about 22 J/g [44]. Estimated from the calorimetric measurements, the mass fraction of NiTi matrix was about 10.05%, which was a little lower than the design composition. This may be due to the extrusion of NiTi matrix during the hot pressing process. It should be indicated that nearly all of the NiTi matrix in W–$Ni_{42}Ti_{53}Nb_5$ composite could undergo inverse martensitic transformation in the W–$Ni_{42}Ti_{53}Nb_5$ composite under thermal cycles.

The morphology of W particles, interface between W and NiTi matrix in the W–$Ni_{42}Ti_{53}Nb_5$ composite were investigated by TEM, as shown in Fig. 6. It can be seen that the typical morphology of most of W particles was round and they were surrounded by NiTi binder. The High-resolution TEM images shown in Fig. 6(c) demonstrated that the interface between W and NiTi matrix was coherent interface. Selected area diffraction (SAD) patterns indicated that the adjacent W and TiNi crystals were of homologous orientation with a small tilting angle. Good bonding between W particles and the NiTi binder was obtained in the composite, which would result in improved performance of mechanical performance [45]. The TEM results further confirmed that no intermediate phase existed at the interface between NiTi binder and W particles.

Based on the analysis above, in order to fabricate two-phase tungsten-based composite containing ductile nearly equiatomic NiTi matrix, equiatomic NiTi alloy is not suitable to be chosen as the master alloy due to the mutual diffusion between NiTi matrix and tungsten and the brittle Ni_3Ti phase forming in the matrix. Increasing the Ti/Ni ratio in binary master alloy to 56: 44 could reduce the content of Ni_3Ti. While when the Ti/Ni ratio increasing to 58: 42, brittle Ti_2Ni phase appeared. In contrast to the binary NiTi master alloy, ternary $Ni_{42}Ti_{53}Nb_5$ seems to be the best candidate to fabricate W–NiTi composites. All the results of XRD, SEM, DSC and TEM suggested that no brittle phases were detected in the NiTi matrix of W–$Ni_{42}Ti_{53}Nb_5$ composite and the matrix consisted of only nearly equiatomic NiTi in martensite state that could undergo reversible martensitic transformation under thermal cycles. Table 2 summarized the phase component and transformation behavior in the four different W–NiTi composites.

The mechanical properties of the four different W–NiTi composites were investigated by compression test at room temperature. Fig. 7(a) and (b) presents the engineering stress-strain curves and the corresponding true stress-true strain curve of the W–$Ni_{42}Ti_{53}Nb_5$ composite. For comparision, the mechanical property of monolithic W under compression at room temperature was also given in Fig. 7(a). The results show that the W–NiTi composites exhibited more excellent mechanical properties than monolithic W due to the introduction different volume fraction of ductile NiTi phase in the matrix. The W–$Ni_{42}Ti_{53}Nb_5$ composite exhibited the largest fracture strain (about 50.4%) and the highest ultimate compressive strength (3820 MPa). Fig. 7(c) shows the overall look of the fractured sample of W–$Ni_{42}Ti_{53}Nb_5$ composite, which showing significant barreling. This indicates a high deformability of the composite at room temperature. It is worthy to note that the W–$Ni_{42}Ti_{53}Nb_5$ composite showed a double yielding phenomenon (as shown in the inset), just as some other composites containing martensite components, such as NiTi/Ti_3Sn, NiTi/Ti_5Si_3, NiTi/Ti_2Ni and NiTi/amorphous metallic composites [16,18–20]. The first yielding occurred at about 760 MPa at the strain of 2.17%, while the second yielding happened at approximate 1500 MPa at the strain of 7.48%. It also can be seen from the true stress-strain curve that the W–$Ni_{42}Ti_{53}Nb_5$ composite underwent obvious strain hardening after the second yielding in Fig. 7(b).

In situ synchrotron HEXRD measurements were conducted to explain deformation mechanism of the W–$Ni_{42}Ti_{53}Nb_5$ composite during compression test. Fig. 8(a) and (b) show one-dimensional diffraction pattern evolutions of the HEXRD peaks of B19'–NiTi and W at different levels of applied stress. It can be seen from the diffraction pattern that the composite consisted of B19'–NiTi and W phases at room temperature, which was consistent with the XRD and DSC results shown in Figs. 2 and 5, respectively.

Upon loading, the B19'–NiTi and W diffraction peaks are initially found shifting to lower d-spacing values, which demonstrated the elastic deformation of both components in the composite under compression at the initial stage of deformation. With the deformation going into the high levels of the applied stress, the d-spacing values of both components remained almost constant or increased very slowly, indicating the plastic deformations. Meanwhile, the diffraction peaks broadening was found with increasing applied stress, which implies the increased inhomogeneity in strain fields which was related to increased defects density [46]. From

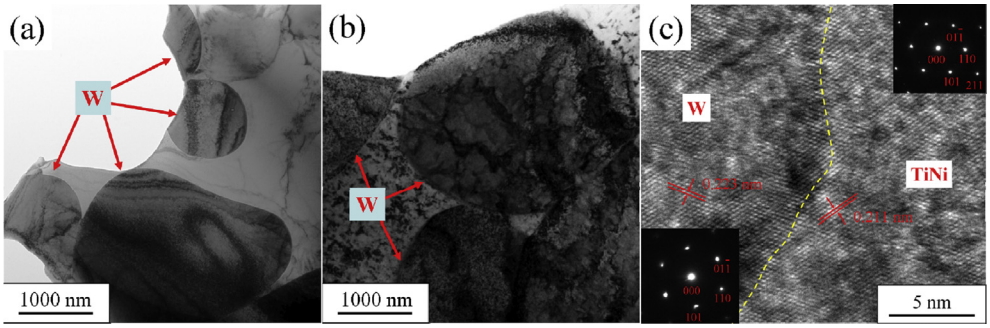

Fig. 6. TEM micrographs of the W–$Ni_{42}Ti_{53}Nb_5$ composite before and after compression. (a) TEM bright field image before compression. (b) TEM bright field image after compression. (c) High-resolution TEM image of the interface and corresponding selected area electron diffraction patterns of NiTi and W of the W–$Ni_{42}Ti_{53}Nb_5$ composite before compression.

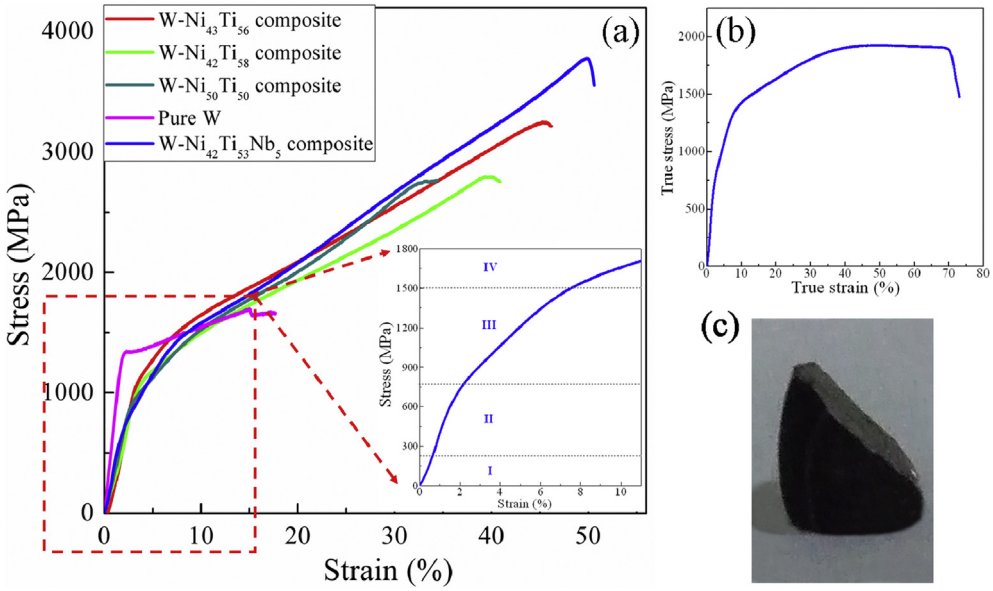

Fig. 7. Mechanical properties of the W–NiTi composites and monolithic W under quasi-static compression at room temperature. (a) Compressive engineering stress-strain curves of the W–NiTi composites and monolithic W under compression. (b) The corresponding true stress-strain curve of the W–$Ni_{42}Ti_{53}Nb_5$ composite. (c) Overall look of the fractured sample showing significant barreling. This indicates a high deformability.

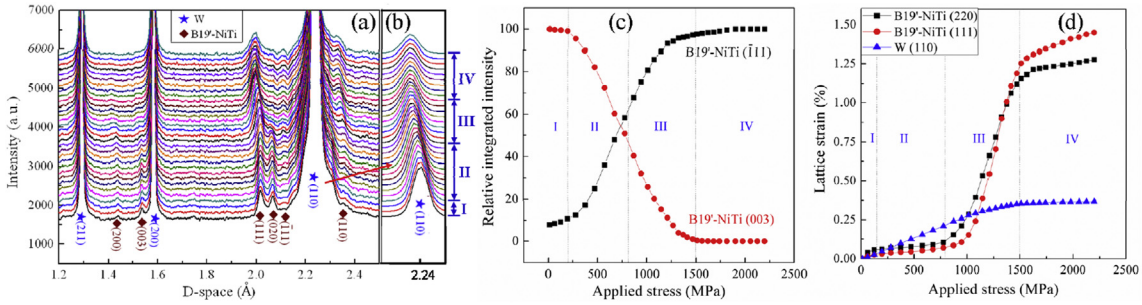

Fig. 8. Microscopic responses of W–$Ni_{42}Ti_{53}Nb_5$ composite revealed by *in situ* synchrotron HEXRD. (a) and (b) One-dimensional diffraction pattern evolutions of the high-energy X-ray diffraction peaks of B19'–NiTi and W at different levels of applied stress in the direction perpendicular to the loading direction. (c) Evolution of relative integrated intensities of the B19'–NiTi (1 11) and B19–NiTi (003) diffraction peaks with the applied stress. (d) Evolution of the lattice strain with respect to the applied stress for the B19'–NiTi (111), B19'–NiTi (220) and W (110) plane perpendicular to the loading direction in the composite.

Fig. 8(a), it also can be seen that the intensity of B19'–NiTi (110) and B19'–NiTi ($\bar{1}$11) diffraction peaks increased whilst the intensity of B19'–NiTi (200), B19'–NiTi (003) and B19'–NiTi (020) diffraction peaks decreased, which indicates that the martensite variant reorients via detwinning. Fig. 8(c) shows the evolution of the relative integrated intensities of the B19'–NiTi (1 11) and B19'–NiTi (003) diffraction peaks along the loading direction as functions of the applied stress. The integrated intensity of the B19'–NiTi (1 11) peak increased and that of B19'–NiTi (003) decreased from the early stage of deformation due to the occurrence of the stress-induced martensite reorientation. The process reached completion at the applied stress of 1500 MPa. This observation demonstrates that the stress-induced martensitic reorientation of the NiTi plays an important role in the initial deformation of the W–NiTi composite.

Fig. 8(d) shows the lattice strain for B19'–NiTi (111), B19'–NiTi (220) and W (110) planes as a function of the applied stress perpendicular to the loading direction. The curve was divided into four stages: <230 MPa (I), 230 MPa–760 MPa (II), 760 MPa-1500 MPa (III), >1500 MPa (IV) of applied stress. The four deformation stages divided in stress-strain curve shown in Fig. 7 are consistent with the deformation stages in Fig. 8. In the elastic zone (stage I, up to 230 MPa in Fig. 8 (d), the lattice strains of W and B19'–NiTi increased linearly fast. For stage II, non-linear responses of the lattice strains to the applied stress were presented for B19'–NiTi. The lattice strain curves of B19'–NiTi (111) and B19'–NiTi (220) displayed a plateau region at the stress of 230 MPa, while the lattice strain of W still increased linearly. According to the previous studies [19], the non-linear nature of the lattice strain curve may be attributed to the occurrence of the martensite reorientation. The stress on the B19' martensite during this stage of deformation was very low, and the increasing external load was mainly borne by the W phase, implying gradual load transfer from NiTi matrix to W particles.

At stage III, from 760 MPa to 1500 MPa, both the lattice strains of W and B19' martensite increased. The sharp increase in the lattice strain of B19' martensite with deformation indicated the commencement of elastic and plastic deformation of the oriented martensite. In contrast to the sharp increasing in the lattice strain of B19' martensite, the W lattice strain continued to increase with the applied stress at a little lower rate. Due to the large volume fraction and the high modulus of W in the composite, the decreasing of the increasing rate of the W lattice strain resulted in a lower increase in external load in this stage, as evident in Fig. 7. This implies the

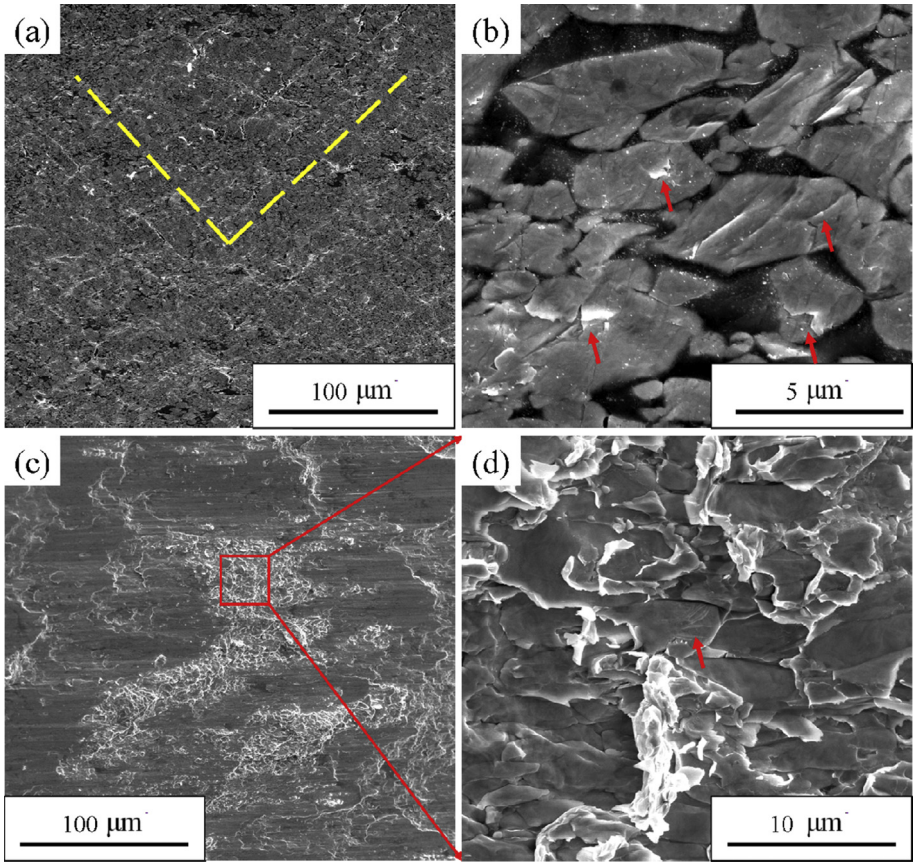

Fig. 9. (a) Low magnification SEM picture of the external surface of the fractured W– $Ni_{42}Ti_{53}Nb_5$ composite. (b) High magnification SEM picture of the external surface of the fractured W–$Ni_{42}Ti_{53}Nb_5$ composite. (c) Low magnification SEM picture of the fracture surface of the W–$Ni_{42}Ti_{53}Nb_5$ composite. (d) High magnification SEM picture of the fractured surface of the W–$Ni_{42}Ti_{53}Nb_5$ composite.

yielding at about 760 MPa on the stress-strain curve was attributed to the martensite reorientation.

At stage IV (up to 1500 MPa), the lattice strains of W (100) and B19'–TiNi (111) continued to increase, but the lattice strain slopes became smaller, which implies the second yielding is obviously due to the commencement of massive plastic deformation of the reoriented martensite and is also attributed to the plastic deformation of the W particles. The further moderate increase in the true stress on the composite Fig. 7(b) is clearly caused by the strain hardening of the B19' martensite and the plastic deformation of tungsten particles, just like that of the *in-situ* NiTi/Ti_5Si_3, NiTi/Ti_3Sn and NiTi/Ti_2Ni composites [16,18,19]. The maximum lattice strain reached in the W (110) of the composite was 0.38% before the fracture of the W–$Ni_{42}Ti_{53}Nb_5$ composite.

TEM observation in Fig. 6(b) revealed that in contrast to as-sintered W–$Ni_{42}Ti_{53}Nb_5$ composite, the deformed sample exhibited tungsten grains with high-density dislocations. The increase of the dislocation density in the tungsten phase is considered to be caused by plastic deformation during compression. The dislocation in tungsten grains could block the farther slippage of the dislocation and increased the fracture strength of W–$Ni_{42}Ti_{53}Nb_5$ composite. The TEM micrograph of the deformed composite further confirmed that the second yielding of the composite was also caused by the plastic deformation of the W particles.

Fig. 9 shows SEM micrographs of the morphology of pre-polished external and fracture surfaces of the W–$Ni_{42}Ti_{53}Nb_5$ composite after compression. It can be seen from Fig. 9(a) that profuse slip bands, inclined by about 45° to the direction of the applied load along the maximum shear plane, were distributed on the lateral surface of the fractured sample. The high magnification SEM picture of the pre-polished lateral surface after deformation in Fig. 9(b) shows that some internal micro-cracks formed in the tungsten particles. The micro-cracks were arrested by the NiTi matrix. The results indicate that the ductile NiTi matrix could effectively hinder the propagation of internal micro-cracks and prevent catastrophe failure of the sample under compression. Fig. 9(c) and (d) are the fracture surface of the W–$Ni_{42}Ti_{53}Nb_5$ composite after compression. Two morphologies of coarse patterns and smooth surface were observed in different regions of compressive fracture surface. The smooth areas were resulted from friction between two fracture surfaces during deformation based on previous reports [47,48]. Fig. 9(d) is high magnification graph of the coarse patterns in Fig. 9(c). It can be seen that the fracture graph of tungsten particle was flat and some river-like pattern (indicated by red arrows) was detected. While for NiTi matrix, severe tearing occurred. No debonding between W particle and NiTi matrix was detected because of the high bonding strength between them.

4. Conclusion

Novel two-phase tungsten-based composites were successfully fabricated by introducing ductile nearly equiatomic NiTi matrix in martensite state by infiltration and hot pressing process. In contrast to the binary NiTi master alloy, ternary $Ni_{42}Ti_{53}Nb_5$ seems to be the best candidate to fabricate W–NiTi composite because no brittle intermetallics formed in the NiTi matrix. The W–$Ni_{42}Ti_{53}Nb_5$ composite exhibits a high ultimate compressive strength and a large plasticity, which overcomes the brittleness of tungsten at

room temperature. NiTi matrix deforming by martensite variant detwinning effectively hindered the propagation of micro-cracks in tungsten particles and prevented catastrophe failure of the composite under compression.

Acknowledgment

This work was supported by the key program project of the National Natural Science Foundation of China (NSFC) (51231008), the National 973 program of China (2012CB619403), the NSFC (11474362 and 51571212).

References

[1] E. Lassner, W.-D. Schubert, Tungsten: Properties, Chemistry, Technology of the Element, Alloys, and Chemical Compounds, Springer Science & Business Media, 2012.
[2] S. Wurster, N. Baluc, M. Battabyal, T. Crosby, J. Du, C. García-Rosales, A. Hasegawa, A. Hoffmann, A. Kimura, H. Kurishita, R.J. Kurtz, H. Li, S. Noh, J. Reiser, J. Riesch, M. Rieth, W. Setyawan, M. Walter, J.H. You, R. Pippan, Recent progress in R&D on tungsten alloys for divertor structural and plasma facing materials, J. Nucl. Mater. 442 (2013) S181–S189.
[3] J. Reiser, M. Rieth, B. Dafferner, A. Hoffmann, Tungsten foil laminate for structural divertor applications – basics and outlook, J. Nucl. Mater. 423 (2012) 1–8.
[4] J. Reiser, M. Rieth, A. Möslang, B. Dafferner, J. Hoffmann, T. Mrotzek, A. Hoffmann, D.E.J. Armstrong, X. Yi, Tungsten foil laminate for structural divertor applications – joining of tungsten foils, J. Nucl. Mater. 436 (2013) 47–55.
[5] C.H. Henager, R.J. Kurtz, T.J. Roosendaal, B.A. Borlaug, W. Setyawan, K.B. Wagner, G.R. Odette, K. Cunningham, K.A. Fields, D. Gragg, in: Recent Progress in the Development of Ductile-phase Toughened Tungsten for Plasma-facing Materials, Pacific Northwest National Laboratory (PNNL), Richland, WA (US), 2014.
[6] Y. Şahin, Recent progress in processing of tungsten heavy alloys, J. Powder Techno. 2014 (2014) 1–22.
[7] O. Dinçer, M.K. Pehlivanoğlu, N.K. Çalişkan, İ. Karakaya, A. Kalkanli, Processing and microstructural characterization of liquid phase sintered tungsten–nickel–cobalt heavy alloys, Int. J. Refract. Met. Hard Mater 50 (2015) 106–112.
[8] H. Liu, S. Cao, J. Zhu, Y. Jin, B. Chen, Densification, microstructure and mechanical properties of 90W–4Ni–6Mn heavy alloy, Int. J. Refract. Met. Hard Mater 37 (2013) 121–126.
[9] X. Fang, J. Liu, X. Wang, S. Li, L. Zheng, Study on improving “self-sharpening” capacity of W–Cu–Zn alloy by the pressureless infiltration method, Mater. Sci. Eng. A 607 (2014) 454–459.
[10] S. Islam, X. Qu, S. Askari, M. Tufail, X. He, Effect of microstructural parameters on the properties of W-Ni-Fe alloys, Rare Met. 26 (2007) 200–204.
[11] S.H. Islam, X. Qu, X. He, Investigation of composition and microstructure effect on fracture behaviour of tungsten heavy alloys, Powder Metall. 50 (2013) 11–13.
[12] B. Rabin, R. German, Microstructure effects on tensile properties of tungsten-nickel-iron composites, Metall. Trans. A 19 (1988) 1523–1532.
[13] I.S. Humail, F. Akhtar, S.J. Askari, M. Tufail, X. Qu, Tensile behavior change depending on the varying tungsten content of W–Ni–Fe alloys, Int. J. Refract. Met. Hard Mater 25 (2007) 380–385.
[14] R. Woodward, R. O'Donnell, Tensile rupture of tungsten alloys by the cascade of crack nucleation events, J. mater. Sci. 35 (2000) 4067–4072.
[15] K. Knipling, G. Zeman, J. Marte, S. Kelly, S. Kampe, Effect of dissolved tungsten on the deformation of 70Ni-30Fe alloys, Metall. Mater. Trans. A 35 (2004) 2821–2828.
[16] J. Zhang, L. Cui, D. Jiang, Y. Liu, S. Hao, Y. Ren, X. Han, Z. Liu, Y. Wang, C. Yu, Y. Huan, X. Zhao, Y. Zheng, H. Xu, X. Ren, X. Li, A biopolymer-like metal enabled hybrid material with exceptional mechanical prowess, Sci. Rep. 5 (2015) 8357.
[17] F. Qiu, P. Shen, C. Liu, Q. Jiang, Effects of Ni addition on the microstructure and compressive deformation behavior in Zr–Cu–Ni martensitic alloys, Mater. Des. 34 (2012) 143–147.
[18] Y.F. Sun, B.C. Wei, Y.R. Wang, W.H. Li, T.L. Cheung, C.H. Shek, Plasticity-improved Zr–Cu–Al bulk metallic glass matrix composites containing martensite phase, Appl. Phys. Lett. 87 (2005) 051905.
[19] J. Zhang, Y. Liu, Y. Ren, Y. Huan, S. Hao, C. Yu, Y. Shao, Y. Ru, D. Jiang, L. Cui, In situ synchrotron X-ray diffraction study of deformation behavior and load transfer in a Ti_2Ni-NiTi composite, Appl. Phys. Lett. 105 (2014) 041910.
[20] D. Jiang, S. Hao, J. Zhang, Y. Liu, Y. Ren, L. Cui, In situ synchrotron investigation of the deformation behavior of nanolamellar Ti_5Si_3/TiNi composite, Scr. Mater. 78–79 (2014) 53–56.
[21] K. Otsuka, X. Ren, Physical metallurgy of Ti–Ni-based shape memory alloys, Prog. Mater Sci. 50 (2005) 511–678.
[22] B.T. Lester, T. Baxevanis, Y. Chemisky, D.C. Lagoudas, Review and perspectives: shape memory alloy composite systems, Acta Mech. 226 (2015) 3907–3960.
[23] M. Bitzer, M. Bram, H.P. Buchkremer, D. Stöver, Phase transformation behavior of hot isostatically pressed NiTi-X (X = Ag, Nb, W) alloys for functional engineering applications, J. Mater. Eng. Perform. 21 (2012) 2535–2545.
[24] S. Wang, F.M. Guo, D.Q. Jiang, Y. Liu, L.S. Cui, In situ W–NiTi shape memory alloy composite of high radiopacity, Scr. Mater. 81 (2014) 4–7.
[25] A.C. Kneissl, K. Mehrabi, M. Bruncko, B.J. McKay, D. Uhlenhaut, Characterization and properties of NiTi(W) and CuAlNi shape memory alloys, Int. J. Mater. Res. 100 (2009) 1038–1045.
[26] K. Mehrabi, H. Bahmanpour, A. Shokuhfar, A. Kneissl, Influence of chemical composition and manufacturing conditions on properties of NiTi shape memory alloys, Mater. Sci. Eng. A 481–482 (2008) 693–696.
[27] M. Nishida, C.M. Wayman, T. Honma, Precipitation processes in near-equiatomic TiNi shape memory alloys, Metall. Trans. A 17 (1986) 1505–1515.
[28] Winston O. Soboyejo, T.S. Srivatsan, Advanced Structural Materials: Properties, Design Optimization, and Applications, CRC Press, 2006.
[29] T.-H. Nam, J.-H. Lee, D.-W. Jung, C.-A. Yu, Y. Liu, Y.-W. Kim, Transformation behaviour of Ti–Ni and Ti–Ni–Cu alloy ribbons with nano Ti2Ni particles, Mater. Sci. Eng. A 449–451 (2007) 1041–1044.
[30] X.X. Zhang, H.W. Hou, L.S. Wei, Z.X. Chen, W.T. Wei, L. Geng, High damping capacity in porous NiTi alloy with bimodal pore architecture, J. Alloys Compd. 550 (2013) 297–301.
[31] M. Kaya, N. Orhan, G. Tosun, Phase transformation behaviours of porous NiTi SMA fabricated as hollow and solid cylinders by SHS, Mater. Sci. Technol. 26 (2013) 522–527.
[32] S.F. Hsieh, S.K. Wu, H.C. Lin, C.H. Yang, Transformation sequence and second phases in ternary Ti–Ni–W shape memory alloys with less than 2 at.% W, J. Alloys Compd. 387 (2005) 121–127.
[33] H. Shi, S. Pourbabak, J. Van Humbeeck, D. Schryvers, Electron microscopy study of Nb-rich nanoprecipitates in Ni–Ti–Nb and their influence on the martensitic transformation, Scr. Mater. 67 (2012) 939–942.
[34] M. Piao, S. Miyazaki, K. Otsuka, N. Nishida, Effects of Nb addition on the microstructure of Ti–Ni alloys, Mater. Trans. JIM 33 (1992) 337–345.
[35] L. Wei, Z. Xinqing, Mechanical properties and transformation behaviour of NiTiNb shape memory alloys, Chin. J. Aeronaut. 22 (2009) 540–543.
[36] X. Fu, M. Guojun, Z. Xinqing, X. Huibin, Effects of Nb content on yield strength of NiTiNb alloys in martensite state, Chin. J. Aeronaut. 22 (2009) 658–662.
[37] J. Li, H. Wang, J. Liu, J. Ruan, Effects of Nb addition on microstructure and mechanical properties of TiNiNb alloys fabricated by elemental powder sintering, Mater. Sci. Eng. A 609 (2014) 235–240.
[38] M. Hansen, K. Anderko, H. Salzberg, Constitution of binary alloys, J. Electrochem. Soc. 105 (1958) 260C–261C.
[39] A. Upadhyaya, Processing strategy for consolidating tungsten heavy alloys for ordnance applications, Mater. Chem. Phys. 67 (2001) 101–110.
[40] A.P. Hammersley, S.O. Svensson, M. Hanfland, A.N. Fitch, D. Hausermann, Two-dimensional detector software: from real detector to idealised image or two-theta scan, High Press. Res. 14 (1996) 235–248.
[41] Y. Zhang, X. Cheng, H. Cai, Fabrication, characterization and tensile property of a novel Ti2Ni/TiNi micro-laminated composite, Mater. Des. 92 (2016) 486–493.
[42] P.J.S. Buenconsejo, R. Zarnetta, D. König, A. Savan, S. Thienhaus, A. Ludwig, A new prototype two-phase (TiNi)-(β-W) SMA system with tailorable thermal hysteresis, Adv. Funct. Mater. 21 (2011) 113–118.
[43] K. Enami, M. Hara, H. Maeda, Effect of W addition on the martensitic transformation and shape memory behaviour of the TiNi-base alloys, J. Phys. IV 5 (1995). C8–629-C628-633.
[44] D. Cluff, S.F. Corbin, The influence of Ni powder size, compact composition and sintering profile on the shape memory transformation and tensile behaviour of NiTi, Intermetallics 18 (2010) 1480–1490.
[45] D.R. Ni, J.J. Wang, Z.N. Zhou, Z.Y. Ma, Fabrication and mechanical properties of bulk NiTip/Al composites prepared by friction stir processing, J. Alloys Compd. 586 (2014) 368–374.
[46] A.K. Kanjarla, R.A. Lebensohn, L. Balogh, C.N. Tomé, Study of internal lattice strain distributions in stainless steel using a full-field elasto-viscoplastic formulation based on fast Fourier transforms, Acta Mater. 60 (2012) 3094–3106.
[47] S. Jayalakshmi, S. Sahu, S. Sankaranarayanan, S. Gupta, M. Gupta, Development of novel Mg–Ni60Nb40 amorphous particle reinforced composites with enhanced hardness and compressive response, Mater. Des. 53 (2014) 849–855.
[48] S. Sankaranarayanan, V. Hemanth Shankar, S. Jayalakshmi, N. Quy Bau, M. Gupta, Development of high performance magnesium composites using Ni50Ti50 metallic glass reinforcement and microwave sintering approach, J. Alloys Compd. 627 (2015) 192–199.